Hainzl, S., Ben-Zion, Y., Cattania, C., Wassermann, J. (2013): Testing atmospheric and tidal earthquake triggering at Mt. Hochstaufen, Germany. - *Journal of Geophysical Research*, *118*, 10, 5442-5452

DOI: 10.1002/jgrb.50387

JOURNAL OF GEOPHYSICAL RESEARCH: SOLID EARTH, VOL. 118, 5442–5452, doi:10.1002/jgrb.50387, 2013

Testing atmospheric and tidal earthquake triggering at Mt. Hochstaufen, Germany

S. Hainzl,[1] Y. Ben-Zion,[2] C. Cattania,[1] and J. Wassermann[3]

Received 22 May 2013; revised 24 September 2013; accepted 25 September 2013; published 17 October 2013.

[1] Seismicity closely related to hydrological impacts has been observed in several locations worldwide, particularly in intraplate areas where tectonic stressing rates are small. The triggering mechanism is usually explained by a poroelastic response of the seismogenic crust to surface water flux, leading to pore pressure changes at depth. To explain the earthquake triggering in response of those small stress changes, however, the crust has to be near a critical state in which other transient processes might be significant. One of the prominent examples is at Mt. Hochstaufen in SE Germany, where seismicity is known to vary seasonally. A previous analysis showed that the seismicity in 2002 was highly correlated with model forecasts based on fluid diffusion and rate- and state-dependent frictional nucleation. Here we revisit this case by accounting additionally for poroelastic effects, as well as for thermoelastic and tidal stresses. We also test whether the model can explain the observations of the subsequent 8 years between 2003 and 2010. Our analysis confirms that rainfall is the dominant driving force in this region. The model not only fits the year 2002 activity very well but also provides with the same parameters a reasonable fit to the subsequent period, with a probability gain of about 4 per event in comparison to a time-independent Poisson model.

Citation: Hainzl, S., Y. Ben-Zion, C. Cattania, and J. Wassermann (2013), Testing atmospheric and tidal earthquake triggering at Mt. Hochstaufen, Germany, *J. Geophys. Res. Solid Earth*, *118*, 5442–5452, doi:10.1002/jgrb.50387.

1. Introduction

[2] Hydromechanical coupling has been proposed to explain some parts of observed crustal seismicity referred to as hydroseismicity [*Costain and Bollinger*, 2010]. A widely accepted view is that an increase of the pore fluid pressure reduces the effective normal stress and thus the strength of faults, promoting earthquake failure. Direct evidence for fluids affecting the stability of faults comes from reservoir-induced seismicity [*Talwani*, 1997] and fluid injections in wells [*Zoback and Harjes*, 1997; *Shapiro et al.*, 2003; *Fischer et al.*, 2008] where induced pore pressure changes are usually high. However, much lower stresses induced by rainfall have also been reported to trigger seismicity [*Muco*, 1995; *Hainzl et al.*, 2006; *Kraft et al.*, 2006b; *Svejdar et al.*, 2011]. For example, *Hainzl et al.* [2006] found that isolated seismicity which occurred in 2002 below Mt. Hochstaufen, SE Germany, can be very well modeled by pore pressure diffusion and rate- and state-dependent frictional nucleation. That analysis also suggested a very high sensitivity of the crust to minute stress changes. In such near-critical states, however, other processes leading to comparable stress changes might also be important for earthquake triggering. In particular, seasonal variations of the surface temperature are known to induce thermoelastic strain in the underlying rocks [e.g., *Ben-Zion and Leary*, 1986; *Prawirodirdjo et al.*, 2006] and Earth tides can induce stresses large enough to potentially trigger earthquakes in critically stressed regions [e.g., *Thomas et al.*, 2009].

[3] To quantify the roles of tectonic and transient nontectonic-triggering processes, we revisit the activity at Mt. Hochstaufen in 2002, with analysis including additional stress components consistently in the framework of rate- and state-dependent frictional nucleation. Specifically, we consider poroelastic effects and possible accumulation of rain water in open fractures as suggested by *Miller* [2008], along with thermoelastic strain and Earth tides. To test the performance of our model, we run a forecast test for the subsequent 8 years of observations which were not used to calibrate the model. The resulting information gains and correlation coefficients show that atmospheric input data have a significant potential for probabilistic earthquake forecasts at Mt. Hochstaufen. The rainfall provides the main triggering mechanism at the examined site, the thermoelastic strain adds variations that improves the performance of the seismicity model, and the tidal stress does not appear to play a meaningful role.

[4] The remainder of the paper is organized in the following way: In section 2 we introduce the analyzed data and in section 3 we run a test to verify that the earthquake occurrence is nonstationary. In the subsequent section 4

---

[1] GFZ German Research Centre for Geosciences, Potsdam, Germany.

[2] University of Southern California, Los Angeles, California, USA.

[3] Department of Earth and Environmental Sciences, Ludwig-Maximilians-University, Munich, Germany.

Corresponding author: S. Hainzl, GFZ German Research Centre for Geosciences, Potsdam, Germany. (hainzl@gfz-potsdam.de)

2169-9313/13/10.1002/jgrb.50387

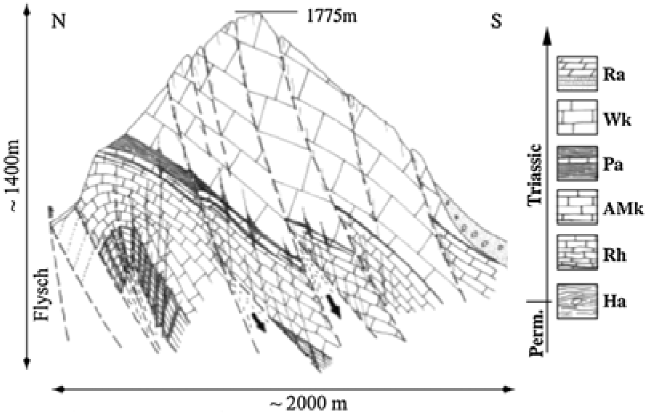

Figure 1. Schematic cross section through Mt. Hochstaufen, showing the thrusting of the Triassic nappes from the South on the Flysch unit in the North. Prominent thrust surfaces are marked schematically as dashed lines. Possible recent movements are indicated by black arrows. Ra: Raibler Formation; Wk: Wettersteinkalk (Limestone); Pa: Partnach Formation; AMk: Alpine Muschelkalk (Limestone); Rh: Reichenhall Formation; Ha: Haselgebirge. Modified after *Weede* [2002].

we explain the computation of the different stress mechanisms and the model approach to account for those transient stresses in the framework of rate- and state-dependent friction. In the final sections we present, discuss, and summarize the results of applying our general approach to the examined data set of Mt. Hochstaufen.

2. Study Area and Input Data

[5] The Staufen massif is located near the city of Salzburg (Austria) and directly northwest of the city of Bad Reichenhall (Germany). Mt. Hochstaufen (1775 m) is the summit of this approximately east-west striking mountain belt which belongs geologically to the Eastern Limestone Alps. The morphology of the Staufen massif is characterized by its pronounced relief with a maximum height difference of 1400 m at only 2000 m base length (Figure 1). The geological units are described as subsequent stratigraphic layers of triassic age which consist mainly of limestone and dolomite as well as interstratified marl and sandstones [*Weede*, 2002]. These units of which the uppermost parts are slightly karstified are thrusted over the cretaceous Flysch zone (Figure 1). The latter unit is composed of marine sedimentary rocks of sandstones, siltstones, and claystones. Interstratified between both geological main units is a late Permian evaporitic breccia (Haselgebirge), which can be found at the northern border of the massif as well as in the basin of Bad Reichenhall and can presumably also be found in the inner fold of the Staufen massif. The Staufen massif shows impressive signs of slope movement and instabilities mostly at the summit crest region. *Weede* [2002] described the deep reaching fractures as consequence of tectonic activity during the thrusting period and the still ongoing relaxation.

[6] A permanent seismic network around Mt. Hochstaufen has been completed in 2004 with seven digital short-period seismic stations (Figure 2). We analyze the local seismicity recorded between 2002 and 2010, during which 1694 events with $M \geq -1$ had been observed with varying station configuration and number. The frequency-magnitude plot of these events is shown in Figure 3a. The completeness magnitude is estimated as $M_c = 0.2$ using the "goodness of fit" approach [*Svejdar et al.*, 2011], resulting in a complete data set of 859 events. We incorporate in the analysis information from a catalog of focal mechanisms for events in 2002 [*Kraft et al.*, 2006b]. This list consists of source parameters for 25 earthquakes with a variance less then 20° of the fault plane normals, i.e., 50 mechanisms related to two possible solutions for each event.

[7] In addition to earthquake data, we use rainfall and temperature measurements in this region. Local meteorological stations (rain gauge, air pressure, air temperature, and humidity) have been colocated at three sites since mid-2004 (RJOB, RNON, and RMOA; see Figure 2). For our analysis we use average values of these stations after this time and measurements of other regional stations before. To avoid a bias due to different station altitudes before and after 2004, we calculated the average offset between the latter and the former measurements during overlapping time periods and corrected the data before 2004 accordingly.

[8] The average rainfall is around 1850 mm/year with approximately twice as much rain in summer as in winter. Two periods of heavy rainfall with more than 100 mm/day occurred in the summers of 2002 and 2005. The average temperature difference between summer and winter is around 25° Celsius (see Figure 3b).

3. Statistical Test for Transient Forcing

[9] Before examining the potential impact of meteorological changes and Earth tides on earthquakes in the study area, we check that the seismicity cannot be simply explained by constant tectonic forcing and earthquake-induced stress changes. For this purpose, we apply the recent approach of *Marsan et al.* [2013], which has been further tested and applied by *Hainzl et al.* [2013]. The method attempts to separate background forcing rate $r(t)$ and aftershock triggering $\nu(t)$ related to earthquake-earthquake interactions, where the observed earthquake rate $\lambda(t)$ is assumed to be a linear superposition of both terms, $\lambda(t) = r(t) + \nu(t)$. The interaction term $\nu(t)$ is modeled using the epidemic type aftershock sequence model [*Ogata*, 1988]

$$\nu(t) = \sum_{i:t_i<t} K e^{\alpha(M_i - M_c)} (c + t - t_i)^{-p} , \tag{1}$$

where t_i and $M_i \geq M_c$ are the occurrence times and magnitudes of the observed earthquakes. The parameters c and p are related to the Omori-Utsu aftershock decay law [*Utsu et al.*, 1995], while K and α describe the magnitude-dependent aftershock productivity. All parameters are estimated by the maximum likelihood method, yielding the optimal parameters $c = 2.1$ s, $p = 1.03$, $K = 0.0036$, and $\alpha = 1.1$, which are in the range of values observed at tectonic plate boundaries. Based on the Akaike Information Criterion (AIC), we find that the background forcing term $r(t)$ is significantly time dependent and accounts for 82% of the activity, that is, only 18% of the earthquakes are identified as aftershocks. The estimated activity related to the background forcing term is shown in Figure 3c, clearly indicating transient (time-dependent) behavior.

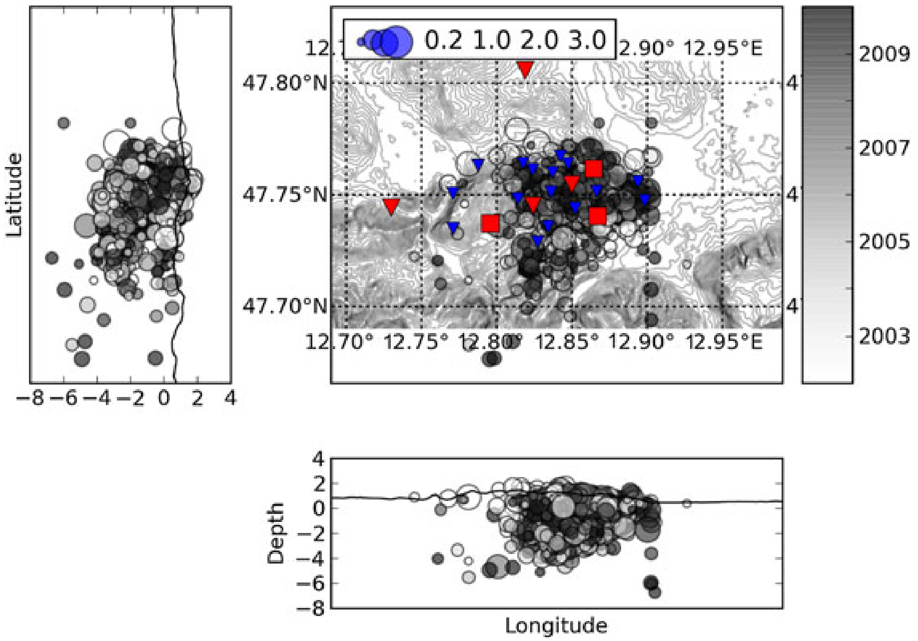

Figure 2. Map of the Staufen Massif as well as EW and NS profiles through the summit of Mt. Hochstaufen with the located earthquakes in the years between 2002 and 2010 (dots). Blue triangles represents the maximum station coverage during 2009. Red triangles are the permanent stations, and squares are the permanent stations with a weather station.

4. Seismicity Model

[10] A widely applied earthquake generation model accounting for rate- and state-dependent frictional nucleation observed in experimental data has been introduced by *Dieterich* [1994]. The main assumptions of this model is that a large number of potential nucleation sites exist in any volume and that earthquakes are nucleating independently of each other. The earthquake nucleation rate R depends on the state variable γ, the constant tectonic background stressing rate $\dot{S}$, and the background seismicity rate r according to

$$R = \frac{r}{\gamma \dot{S}} \,. \tag{2}$$

The evolution of the state variable is governed by

$$d\gamma = \frac{1}{A\sigma}[dt - \gamma dS] \,, \tag{3}$$

with S being the Coulomb Failure stress, σ is the effective normal stress, and A is a dimensionless fault constitutive friction parameter usually estimated as $\sim$0.01 [*Dieterich*, 1994; *Dieterich et al.*, 2000].

[11] The Coulomb Failure Stress is calculated by

$$S = \tau + \mu_{\mathrm{eff}}(\sigma_{\mathrm{n}} + p) \,, \tag{4}$$

with effective friction coefficient $\mu_{\mathrm{eff}} = (\mu - \alpha')$, where α' is a dimensionless constant having typical laboratory values in the range 0.25–0.5. In (4), τ is the shear stress in the direction of slip on the assumed causative fault plane, σ_{n} is the normal stress changes (positive for unclamping or extension), and p is the pore pressure [*King and Cocco*, 2001]. Assuming an isotropic poroelastic model, the pore pressure depends on the volumetric stress and is given by

$$p = -B(\sigma_{11} + \sigma_{22} + \sigma_{33})/3 \,, \tag{5}$$

where B is the Skempton coefficient which varies between 0 and 1 and σ_{ij} defines the stress tensor [*Cocco and Rice*, 2002]. For a local coordinate system with x, y, and z axes denoting the north, east, and up, respectively, the projection of the stress tensor yields

$$\begin{aligned} \tau = {} & -ac(bf + ade)\sigma_{11} + c(2abde + f - 2a^2 f)\sigma_{12} \\ & + (ae - 2ac^2 e + bdf)\sigma_{13} + c(abf - b^2 de)\sigma_{22} \\ & + (adf - be - 2bc^2 e)\sigma_{23} + cde\sigma_{33} \end{aligned} \tag{6}$$

$$\begin{aligned} \sigma_{\mathrm{n}} = {} & 4abcd\sigma_{11} - 2abc^2\sigma_{12} - 2acd\sigma_{13} + b^2c^2\sigma_{22} \\ & + 2bcd\sigma_{23} + d^2\sigma_{33} \end{aligned} \tag{7}$$

with a = sin(strike), b = cos(strike), c = sin(dip), d = cos(dip), e = sin(rake), and f = cos(rake) related to a given earthquake mechanism [*Xu et al.*, 2010].

[12] For an arbitrary stressing history $S(t)$ consisting of a transient stress changes $\triangle S(t)$ in addition to the constant tectonic loading rate $\dot{S}$, the evolution of γ can be tracked by considering sufficiently small time steps leading to stress increments of $\Delta S(t)$ during time intervals of Δt. Implementing the stress step in the center of the time step Δt, the state variable is iterated according to

$$\gamma(t + \Delta t) = \left(\gamma(t) + \frac{\Delta t}{2A\sigma}\right) \exp\left(-\frac{\dot{S}\Delta t + \triangle S(t)}{A\sigma}\right) + \frac{\Delta t}{2A\sigma} \,, \tag{8}$$

starting from the background level, that is, $\gamma(0) = 1/\dot{S}$ [*Hainzl et al.*, 2010].

[13] While tectonic forces alone would produce a continuous stress change with constant stressing rate, our test in section 3 shows that the background stressing rate at Mt. Hochstaufen between the years 2002 and 2010 is strongly time dependent. In the following, we explore the potential

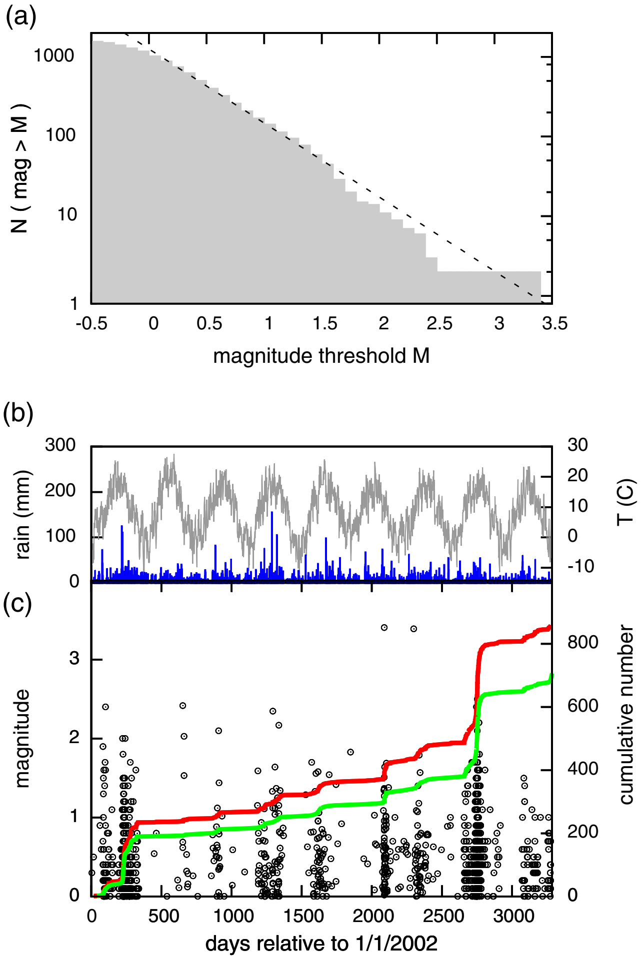

Figure 3. (a) Frequency-magnitude distribution of the earthquakes at Mt. Hochstaufen in the time period 2002–2010. The dashed line refers to a b value of 0.93. (b) Observed daily rainfall (blue) and temperature (grey). (c) Earthquake magnitude and number versus time. The curves (with labels on the right) show the cumulative number of observed $M \geq 0.2$ events (red line) and the fraction related to background activity (green line).

impact of meteorological and tidal stress changes on the recorded seismicity.

4.1. Rainfall-Induced Stress Changes

[14] The ground water level changes are estimated by a simple groundwater model, where the temporal change of the water table dW/dt is assumed to be equal to the difference between recharge rate Q (rainfall) and the ground water discharge rate D. The latter depends on the unknown depth of the water head z according to $D = D_{\max} \exp(-\eta z)$ [*Niu et al.*, 2007]. In agreement with *Niu et al.* [2007], we set the parameters to $\eta = 1.25$ m^{-1} and $D_{\max} = 4.5 \cdot 10^{-4}$ mm s^{-1}. We run the groundwater model for the rainfall data starting from 1995 to avoid transient effects due to the unknown initial conditions and cut the first 4 years. We also tested a simpler model where the change of the ground water level is just equal to the deviation of the rainfall from the average precipitation rate $\bar{Q}$, namely $dW/dt = Q - \bar{Q}$. We find that our results are not strongly dependent on the groundwater model. We also test the possibility suggested by *Miller* [2008] that the rain water is accumulated in open fractures. Such open fractures are observed in the geology of Mt. Hochstaufen, extending from the surface to depth of at least 100m [*Weede*, 2002]. Assuming that a network of interlinking open fractures resulting from slope sliding or the dissolution of carbonates exists down to the permanent water table, the accumulation of rain in these fractures will result in fluid pressure changes at the water level depth directly proportional to the height of the interconnected water column above the permanent water table. This might lead to an effective amplification factor f_r of the recharge rate, that is, $Q = f_r Q_{\mathrm{rain}}$, where Q_{rain} is the homogeneous rate of the rainfall at the surface. Below we test the values $f_r = 1, 10$, and 100.

[15] We assume that the water table is coupled with an underlying fluid-saturated poroelastic rock. Based on the estimated changes of the groundwater level, we calculate the pore pressure changes at seismogenic depth assuming a 1-D model. We focus on the direct effects of pore pressure variations and ignore effects such as strain-dependent hydraulic diffusivity. While *Hainzl et al.* [2006] only considered pore pressure diffusion in response to the surface water supply, we assume in this study a poroelastic response of a saturated crust as proposed by *Miller* [2008]. In this case, the pore pressure change at depth z in response to a step change of the groundwater level $\triangle W$ at time $t = 0$ can be calculated by [*Roeloffs*, 1988; *Simpson*, 2001]

$$\triangle p(z,t) = \left[(1-\alpha)\, erfc\left(z/\sqrt{4Dt}\right) + \alpha\right] \rho g \triangle W\,, \tag{9}$$

with gravitational acceleration g, water density ρ, and parameter α. The latter is related to the Skempton coefficient B and the Poisson ratio ν as $\alpha = B(1+\nu)/[3(1-\nu)]$. In the subsequent analysis, we assume the standard values $\nu = 0.31$ and $B = 0.5$. By convolution of the groundwater level changes with this response function, we get the pore pressure changes $\triangle p(z,t)$ at depth in response to the measured surface rain. The related time series of Coulomb failure stress changes at depth z is given by $\triangle S_{\mathrm{rain}}(z,t) = \mu_{\mathrm{eff}} \triangle p(z,t)$ according to equation (4).

4.2. Thermoelastic Stress Changes

[16] Thermoelastic strain can be induced by spatiotemporal variations of the surface temperature field with potentially significant amplitudes in places having considerable topography and/or lateral material heterogeneity [*Ben-Zion and Leary*, 1986; *Ben-Zion and Allam*, 2013]. Due to the significant topographic variations in the region of interest

Table 1. Description of Model Parameters

Symbol	Description	Value
B	Skempton coefficient	0.5
ν	Poisson ratio	0.31
G	Shear modulus	30 GPa
μ_{eff}	Effective friction coefficient	0.4
D	Hydraulic diffusivity	0.01, 0.1, 1.0, 10 m^2/s
W_{soil}	Soil width	0, 1, 2, 3 m
f_r	Amplification factor for rainfall	1, 10, 100
$A\sigma$	Frictional resistance	Continuous values
$\dot{S}$	Tectonic stressing rate	Continuous values
r	Constant background rate	Continuous values

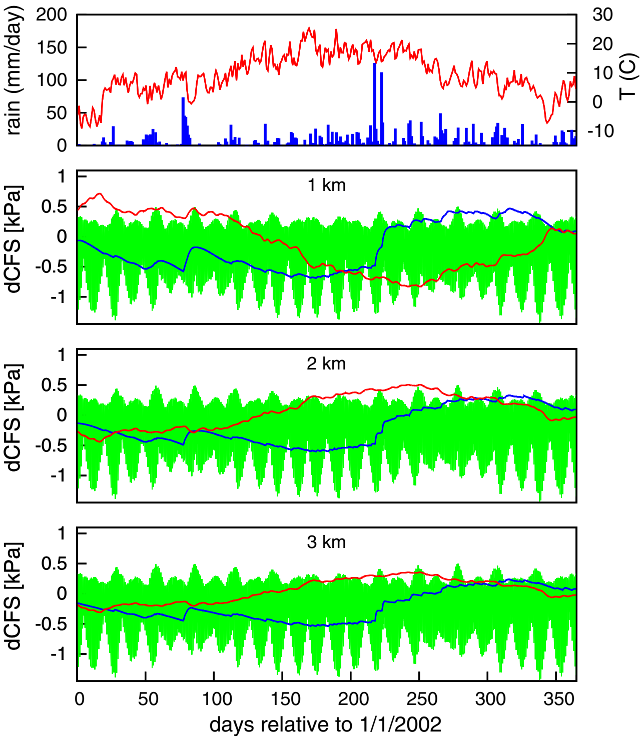

Figure 4. Transient Coulomb stress variations in different depths in response to rainfall (blue curve on top) and temperature (red curve on top) for a receiver mechanism of strike=90°, dip=60° rake=90°. The poroelastic stress changes (blue curves) are calculated with D=1 m^2/s and $f_r = 1$ and the thermoelastic stresses (red curves) are determined with $W_{\text{soil}} = 0$. The green curves show the Coulomb stresses related to Earth tides.

(about 1400 m altitude difference), thermoelastic stresses might be of importance in our case.

[17] An upper layer of loose material might exist and act as a thermoelastic strain insulator, which delays, attenuates, and low-pass filters the surface temperature field. The thermoelastic strain in the underlying half-space can be calculated using the *Berger* [1975] solution and the temperature variations at the base of the decoupled layer. Following *Ben-Zion and Leary* [1986], we assume a stationary spatial cosine variation of the temperature field. Due to the east-west extension of the mountain chain of Mt. Hochstaufen, a standing spatial temperature wave in SN direction with wavelength of about 5 km is a reasonable approximation for the study area. This is expected to produce dominant changes of the horizontal strain ϵ_{11} normal to the topography and related strain $\epsilon_{22} = -\nu\epsilon_{11}$ and $\epsilon_{33} = -\nu\epsilon_{11}$ due to the Poisson's effect. In calculating thermoelastic strain, we use thermal diffusivities of 0.02 m^2/day and 0.04 m^2/day for the unconsolidated layer and the elastic half-space, respectively. Because we have only a point measurement of the temperature rather than different temperature measurements along a south-north profile, we assume that the amplitude of the standing spatial wave can be approximated by the deviations of measured temperatures from the average value. This might be a valid approximation, since the unconsolidated layer is likely significantly thicker in the valley than at the steep slopes of the mountain. In this case, the temperature at the top of the bedrock in the valley will be almost constant at the level of the long-term average value, while the temperature of bedrock in the mountain area will have strong seasonal variations.

[18] The consideration of thermoelastic strain in response to surface temperature variations leads approximately to changes of the stress tensor components $\triangle\sigma_{11} = E\epsilon_{11}$, $\triangle\sigma_{22} = \triangle\sigma_{33} = -\nu E\epsilon_{11}$ at depth, where the Young's modulus E is related to the shear modulus G and the Poisson ratio ν by $E = 2G(1 + \nu)$. Based on these stress changes, the Coulomb Failure stress changes $\triangle S_{\text{thermo}}(z, t)$ in response to the surface temperature changes are calculated by means of equations (4) and (5). In the following, we analyze the results for the induced thermoelastic stresses for cases with and without a soil layer (at the mountain side) by testing soil thicknesses W_{soil} of 0, 1, 2, and 3 m.

4.3. Tidal Forces

[19] We use the SPOTL program package [*Agnew*, 1996] to compute the time series of the horizontal strain (ϵ_{11} and ϵ_{22}) induced by Earth tides. We consider only body tides related to an elastic but oceanless Earth, which is a

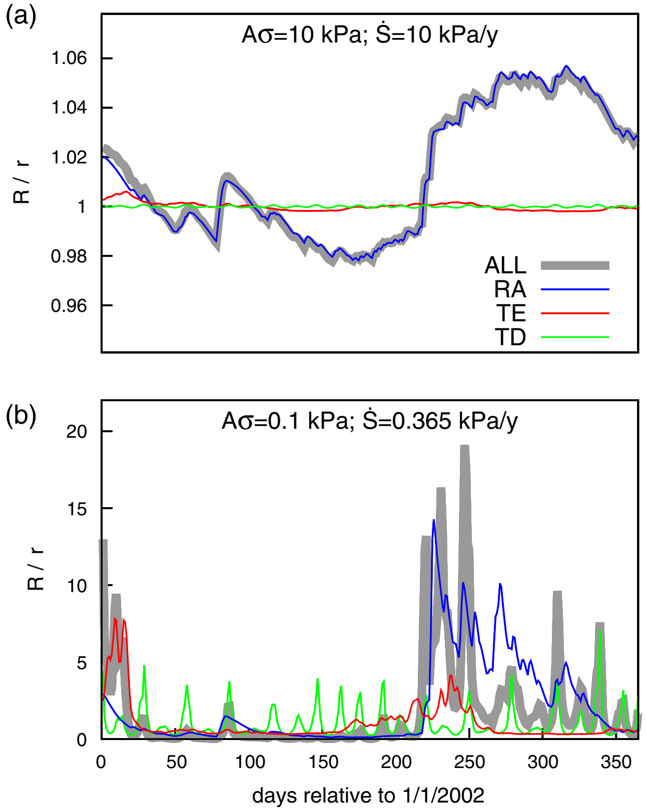

Figure 5. Examples of normalized seismicity rates for two different parameter sets of $A\sigma$ and $\dot{S}$: (a) typical values for plate boundary seismicity and (b) a case of unusually low $A\sigma$ value and stressing rate $\dot{S}$. In the first case, the deviations of the total seismicity rate due to the transient processes are only on the order of a few percent or less, while in the second case, the fluctuations of the seismicity rate become significant. In all cases, the parameters for the underlying stress calculations are the same as for Figure 4.

Table 2. Optimized Model Parameters for the Year 2002[a]

	Model Parameter						Fit Quality[b]		
Model	D (m^2/s)	f_r	W_{soil} (m)	$A\sigma$ (kPa)	$\dot{S}$ (kPa/y)	r (year^{-1})	LL–LL$_{\text{max}}$	C	p_C
RA	10	1/10/100	-	0.16/1.56/15.61	1.0/9.9/98.7	44.8	–1.3	0.72	≥0.999
TE	-	-	0	0.42	0.02	30.9	–129.7	0.33	≥0.999
TD	-	-	-	18.45	96.5	67.1	–192.0	-0.01	0.14
RA + TE	**10**	**1**	**3**	**0.15**	**0.85**	**42.8**	**0.0**	**0.73**	**≥0.999**
ALL	10	1[c]	3	0.25	1.4	50.2	–61.9	0.68	≥0.999
	10	10[c]	3	1.57	9.9	44.8	–2.0	0.72	≥0.999
	10	100	3	15.60	98.6	44.8	–1.3	0.72	≥0.999

[a] The best model is highlighted in bold.

[b] LL = log likelihood value (equation (10)), C = correlation coefficient, and p_C = significance of the correlation.

[c] The parameter is fixed during inversion.

good approximation for this region located several hundreds of kilometers away from the nearest ocean. The resulting Coulomb stress variations $\triangle S_{\text{tidal}}(t)$ related to Earth tides are calculated by means of equations (4) and (5) with stress tensor components $\triangle\sigma_{11} = E\epsilon_{11}$, $\triangle\sigma_{22} = E\epsilon_{22}$, and $\triangle\sigma_{33} = -\nu E(\epsilon_{11} + \epsilon_{22})$.

4.4. Computation Procedure

[20] Table 1 summarizes the model parameters that are used for calculating the stress changes related to the three different mechanisms described above. Examples of calculated stress changes in 2002 based on the local temperature and rainfall records and the estimated solid Earth tides are shown in Figure 4. All three processes lead to stress changes of comparable size on the order of 0.1–1 kPa. However, the stress changes of tides are of a much higher frequency than the rainfall- and temperature-related changes.

[21] We assume that the available focal mechanism catalog is representative for the earthquake mechanisms in the region. For each target receiver mechanism, we calculate a stressing history that is the time series of transient stress changes $\triangle S(z,t)$. To analyze the impact of the different mechanisms, we consider different combinations of the transient processes which are assumed to occur in addition to tectonic loading. For example, if all mechanisms are considered simultaneously, the stress history is $\triangle S(z,t) = \triangle S_{\text{rain}}(z,t) + \triangle S_{\text{thermo}}(z,t) + \triangle S_{\text{tidal}}(t)$. Based on a given stress history $\triangle S(z,t)$, the seismicity rate $R(z,t)$ is calculated by equations (2) and (8) for a given depth z. The total estimated earthquake rate for the assumed earthquake mechanism is calculated by summing the seismicity rate over the different depth levels of the seismogenic zone where the background rate is assumed to be constant. In our case, we scan the depth range between 0.5 and 4.0 km, where most of the earthquakes are located, with step size of 0.5 km. Finally, we average the earthquake rate for all focal mechanisms, leading to an overall seismicity rate $R(t)$.

[22] The rate calculation depends on the model parameters $A\sigma$ and $\dot{S}$. The expected seismicity rates related to the different trigger mechanisms are illustrated in Figure 5 for the year 2002, where two different parameter sets are used. In the first example, we set $A\sigma$ to 10 kPa which is at the lower end of previous estimations for seismicity at plate boundaries; e.g., $A\sigma \approx 20$ kPa for the 1992 M_w 7.3 Landers earthquake [*Hainzl et al.*, 2009]; $A\sigma = 35 \pm 15$ kPa for the 1995 M_w 6.9 Kobe earthquake [*Toda et al.*, 1998]; and $A\sigma = 40$ kPa for the 1997 Umbria-Marche sequence in central Italy [*Catalli et al.*, 2008]. We also set the corresponding tectonic loading rate to $\dot{S} = 10$ kPa/y, in which case a stress-drop event of 1 MPa would have a recurrence time of 100 years. Figure 5a shows that for these parameters, the transient stress changes produce very small effects in all cases, leading to deviations of the seismicity rate of less than 10%. However, the effect becomes significant for smaller frictional resistance values. This is demonstrated in the second example using $A\sigma = 0.1$ kPa and tectonic loading rate of 0.365 kPa/y adapted from results of *Hainzl et al.* [2006]. In this case, the transient processes lead to clear modulations of the seismicity rate (Figure 5b) which should be observable. Note that the effect of the rainfall-induced pore pressure changes is 2–3 times larger than that of thermoelastic or tidal stresses, although all three processes lead to comparable stress amplitudes as can be seen in Figure 4. This can be explained by two different mechanisms: First, earthquake triggering is less sensitive to high-frequency changes than

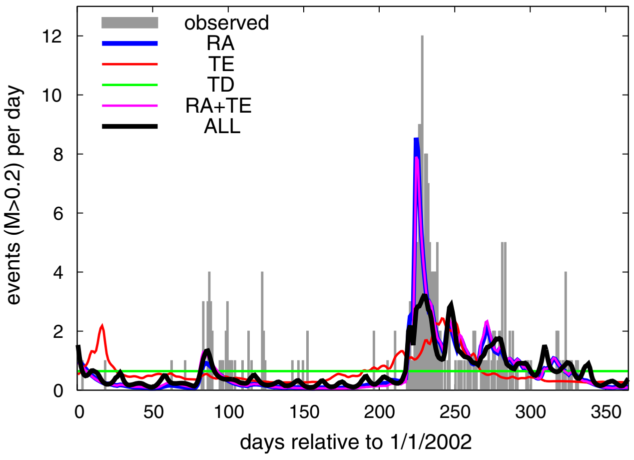

Figure 6. The forecasted number of events per day (curves) in the year 2002 in comparison to the number of observed earthquakes (bars). The corresponding model parameters are given in Table 2, where curves ALL and RA refer to the model with $f_r = 1$. Note that the fit of model ALL with $f_r = 100$ is identical to the RA curve which is itself independent of f_r.

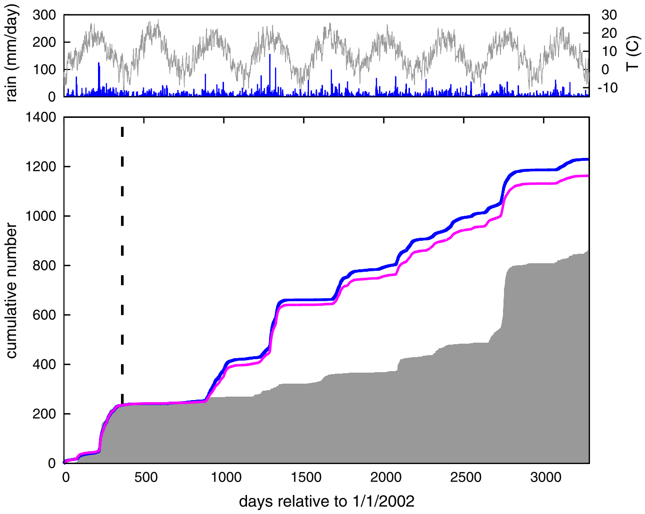

Figure 7. (top) Observed temperature (grey) and rainfall (blue). (bottom) Comparison of the cumulative number of forecasted and observed events. The model forecasts are based on the parameters optimized for 2002 which is marked by the vertical line. The grey-shaded area indicates the observed earthquakes and the curve denote the forecast of ALL model with $f_r = 100$ (blue) and RA + TE model (purple). Note that the forecast of the RA model is identical to the blue curve.

to low-frequency changes, because of the internal time scale of the triggering process, $t_a = A\sigma/\dot{S}$, which acts like a low-pass filter. This explains the reduced effect of tidal stresses. In addition, the rainfall-induced stress changes are identical for all receiver mechanisms and seismicity rates for the different mechanisms are constructively added. In contrast, the changes of the thermoelastic strain compete and increase the stress for some receiver mechanisms but decrease the stress for other mechanisms at the same time. Additionally, the thermoelastic-induced Coulomb stress reverses the sign over the depth range of interest with the assumed wavelength of the temperature field (see, e.g., Figure 4). This leads to activation of a certain receiver mechanisms at one depth interval but to suppression at other depths. Thus, summing the activity for all focal mechanisms and depth levels leads to a significantly smaller net effect. The sign reversal would be eliminated by increasing the wavelength of the temperature field, but we retain a value of 5 km.

[23] To find the best model parameters, we use the maximum likelihood approach to optimize the model fit for the considered time period $[t_s, t_e]$. Assuming that N events occurred in this time period at times t_i ($i = 1, \ldots, N$), the log likelihood value as a function of the parameters $A\sigma$, $\dot{S}$, and r is given by [*Daley and Vere-Jones*, 2003]

$$\begin{aligned}\ln L(A\sigma,\dot{S},r) &= \sum_{i=1}^{N}\ln R(t_i) - \int_{t_s}^{t_e} R(t)\mathrm{d}t \\ &= N\ln(r) - \sum_{i=1}^{N}\ln(\gamma_i\dot{S}) - r\int_{t_s}^{t_e}[\gamma(t)\dot{S}]^{-1}\mathrm{d}t.\end{aligned} \tag{10}$$

Using a grid search for $A\sigma$ and $\dot{S}$, the corresponding value of r can be analytically determined in each case by

$$r = N \Big/ \int_{t_s}^{t_e}[\gamma(t)\dot{S}]^{-1}\mathrm{d}t. \tag{11}$$

5. Results

[24] We analyze the following set of models:

RA: Only rainfall-induced stress changes are considered, $\triangle S = \triangle S_{\mathrm{rain}}$.
TE: Only thermoelastic stresses are considered, $\triangle S = \triangle S_{\mathrm{thermo}}$.
TD: Only tidal stresses are considered, $\triangle S = \triangle S_{\mathrm{tidal}}$.
RA + TE: Rainfall-induced and thermoelastic stress changes are simultaneously considered, $\triangle S = \triangle S_{\mathrm{rain}} + \triangle S_{\mathrm{thermo}}$.
ALL: All processes are considered to occur simultaneously, $\triangle S = \triangle S_{\mathrm{rain}} + \triangle S_{\mathrm{thermo}} + \triangle S_{\mathrm{tidal}}$.

[25] In section 5.1, we first reanalyze the 2002 data, which have been studied before by *Hainzl et al.* [2006], considering also thermoelastic and tidal effects in addition to rainfall-induced poroelastic changes. In particular, we optimize the remaining model parameters for the seismicity recorded in 2002 and rank the different mechanisms according to their fit quality. Afterwards, the model parameters are kept fixed in order to test the models for an independent data set, namely the seismicity that occurred in the subsequent 8 years between 2003 and 2010. The results of these tests are presented in section 5.2.

5.1. Analysis of the 2002 Seismicity

[26] For each analyzed model, we determine parameters that optimize the log likelihood value (equation (10)) for the earthquake activity in 2002 assuming possible rainfall amplification factors of 1, 10, or 100. The resulting parameter values are listed in Table 2, and the corresponding model fits are shown in Figure 6. For the optimized models, we also calculate the linear correlation coefficient C between the daily forecasted and observed number of earthquakes with its significance p_C. The p_C value is the probability that the observed correlation value cannot be explained in the case that model results and observations are uncorrelated.

[27] The best model yielding the highest likelihood value and the highest correlation coefficient of 0.73 is the model

Table 3. Probability Gain per Earthquake and Correlation Coefficient Related to the Daily Earthquake Activity for the Forecast Period 2003–2010[a]

Model	Information Gain	Correlation C	Significance p_C
RA	3.6	0.32	≥0.999
TE	0.7	–0.08	0.998
TD	1.0	–0.005	0.23
RA + TE	4.0	0.33	≥0.999
ALL	3.6	0.32	≥0.999

[a] The result is provided for the different model classes, where parameters were set to those values optimizing the fit to the year 2002 (see Table 2).

RA + TE combining rainfall and thermoelastic effects without rainfall amplification (f_r = 1). Accounting additionally for tidal stresses worsen the model performance. This is indicated by the lower log likelihood value (ΔLL = –61.9) and correlation coefficient (C = 0.68) for model ALL with f_r = 1. The pure rainfall model RA is only slightly worse than the RA + TE model with values ΔLL = –1.3 and C = 0.72. The performance of the RA model is independent of the factor f_r that only rescales the parameter estimation of $A\sigma$ and $\dot{S}$ (see below). However, the consideration of rain water accumulation ($f_r \geq 10$) increases the performance of model ALL which becomes almost identical to model RA. Although significantly worse, the pure thermoelastic TE model still gives a significant positive correlation with the observations ($C \approx 0.3$). In contrast, the tidal TD model does not show any correlation with the observed seismicity. This can be seen in Figure 6. While the best-fitting TD model shows an almost constant rate, all other models are able to explain the time period of main earthquake activity in 2002. In addition, the combined models (RA + TE and ALL) and the pure rainfall model (RA) can explain the rapid onset and subsequent decay of the seismicity in March and August 2002 very well.

[28] In all cases, the best fit yields a high hydraulic diffusivity of $10 m^2/s$ referring to a rapid onset of the activity. In contrast, the estimation of the soil width W_{soil} does not yield the same result for combined models ALL/RA + TE and the pure thermoelastic model TE. On one hand, the best fit is obtained for a negligible soil width in the TE model accounting solely for thermoelastic strain. On the other hand, a rather thick layer of 3 m is preferred in the models combining rainfall and thermoelastic effects simultaneously. Due to the significantly better fit of the latter models, a thicker layer leading to a delayed and reduced stress contribution at depth in response to surface temperature changes is chosen for the subsequent analysis. Concerning the parameters of the rate- and state-dependent frictional nucleation model, the estimation of the background rate is rather stable for the different models (31–67 $M \geq 0.2$ events per year). The two other parameters vary over several orders of magnitude assuming different amplification factors. For example, in model ALL, the estimate of $A\sigma$ increases from approximately 0.2 kPa for f_r = 1 to a value of 16 kPa for f_r = 100. In the latter case, the value is in the range between 10 and 200 kPa, typically found for seismicity in active tectonic areas [*Cocco et al.*, 2010; *Hainzl et al.*, 2010]. Consequently, the local stress state does not have to be exceptionally critical in the area of Mt. Hochstaufen, if rainfall accumulation occurs in open fracture systems. At the same time, the estimation of the tectonic stressing rate increases from 1.4 kPa per year (f_r = 1) to 98.6 kPa per year (f_r = 100). Thus, the estimated time period, which is needed to accumulate 1 MPa, decreases from approximately 700 years to approximately 10 years.

5.2. Forecast of Triggered Seismicity in 2003–2010

[29] Although the models RA and RA + TE fit the 2002 seismicity very well, it has to be considered that several parameters have been optimized for this fit. Thus, it is important to test the models with an independent data set. For this purpose, we now use the earthquake observations of the subsequent 8 years between 2003 and 2010. We compare the model forecasts for this new data set without changing any parameter. The results are presented in Figure 7 for the best-performing models in 2002; i.e., RA + TE, ALL (f_r = 100), and RA. Note that the RA forecast is independent of rain water accumulation (f_r = 1, 10, or 100) and lead to the same result as model ALL with $f_r \geq 10$.

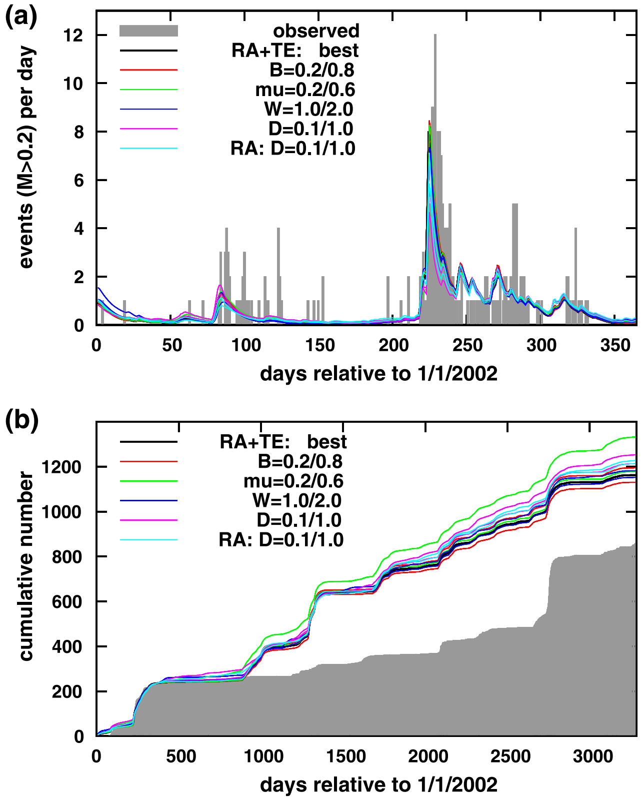

Figure 8. Sensitivity analysis of the results for (a) the 2002 data and (b) the forecast period with respect to changes of the Skempton coefficient (B), effective friction coefficient (μ_{eff}), soil width (W_{soil} in meter), and hydraulic diffusivity (D in m^2/s). The reference is the best-fitting RA + TE model (black) with parameters provided in Table 2, where observations are shown in grey. Note that the upper curve in the forecast period refers to the case of low effective friction of 0.2.

[30] The comparison of the observed and forecasted number of $M \geq 0.2$ earthquakes yields the following results:

[31] 1. The model is able to explain the relative quiescence in the 2 years subsequent to 2002.

[32] 2. Observed and forecasted periods of activation are generally in phase, e.g., intense earthquake activity around 2700 days is explained by the model.

[33] 3. The model fails to forecast the correct amplitudes of the observed swarm activity, e.g., the heavy rainfall that occurred around 1300 days did not trigger as many events as expected from the models. Consequently, the total number is overpredicted by approximately 35%. A possible reason is that surface runoff which is ignored in our model becomes important at that time, because the high model forecast is directly related to one day of extreme rainfall of 155 mm at 11 July 2005, the largest daily amount in the whole-analyzed time period.

[34] To quantify the forecast quality, we calculate the linear correlation coefficient C between the daily forecasted and observed number of earthquakes between 2003 and 2010. In addition, we also determine the probability gain per earthquake relative to forecasts based on a Poisson model which assumes that earthquakes occur with a constant rate. This tests our forecasts based on tectonic plus transient stresses against a model that only accounts for constant tectonic stressing rates. The log likelihood value (equation (10)) for a Poisson model with rate r is given by $\mathrm{LL}_P = N\ln(r) - rT$ for a sample of N events in the time period T. Consequently, the maximum likelihood estimation of the rate r for the year 2002 is just given by $r = N/T = 324$ events per year, and the log likelihood value of the Poisson process for 2003 to 2010 with N'=625 events becomes $\mathrm{LL}_P = 1733$. The probability gain per event is calculated by $\exp[(\mathrm{LL} - \mathrm{LL}_P)/N']$ with LL being the log likelihood value of the forecast model for the period 2003–2010. An information gain larger than one implies that the model forecast is improved compared to the Poisson model, while values below 1 mean a worsening forecast. The resulting values of the probability gain as well as the correlation coefficient are summarized in Table 3. We find that the best-fitting models in 2002 have also the best forecast ability for the seismicity that occurred in the subsequent 8years. In particular, model RA + TE results in an information gain of 4.0. Similarly, model ALL (f_r = 100) and RA as the second best models in 2002 results in the second best result yielding an information gain of 3.6. Although the correlation coefficients are in both cases significantly smaller than in 2002, the values of $C = 0.33$ for RA + TE and $C = 0.32$ for ALL/RA indicate a positive correlation with a significance larger than 99.9%. Interestingly, the correlation and information gain of the TE model are negative, while the contribution of TE strain in the RA + TE model increases the performance compared to the RA model alone. This indicates that TE strain is responsible for a secondary, delayed component of stress variation which drives the observed seismicity. In contrast, the TD mechanism does not significantly contribute because of its short period. We note that the TE strain may also play an additional role related to changes of temperature at depth induced by percolation of rain water, but we do not attempt to model this effect here.

6. Discussion

[35] We tested the sensitivity of our results to parameter changes and uncertainties of the involved focal mechanisms. As a reference model, we choose the RA + TE model with parameters provided in Tables 1 and 2 as the best-fitting model in our analysis. Specifically, we analyzed variations of the Skempton coefficient (B = 0.2 and 0.8 instead of 0.5), the effective friction coefficient (μ_{eff} = 0.2 and 0.6 instead of 0.4), the hydraulic diffusivity value (D = 0.1 and 1 instead of 10 m^2/s), and the soil width (W_{soil} = 1 and 2 instead of 3 m). As discussed in section 5.1, we already know that the RA + TE model converges in the case of significant rain accumulation (f_r) just to the RA model. In each case, we changed one of these parameters and adapted the parameters of the seismicity model ($A\sigma$, $\dot{S}$, and r) by fitting the 2002 data. The results are shown in Figure 8. We find that the fit of the 2002 data as well as the forecast for the period 2003–2010 are rather robust with respect to the parameter changes, with information gains between 3.4 and 4.1 for the forecast period. This indicates that parameter estimations, in particular, for the hydraulic diffusivity coefficient, are not well constrained by the data. The variation of D over two orders of magnitude leads only to minor changes of the fit quality. This is because we did not performed a full spatiotemporal fit of the earthquake data. Due to the varying quality of the hypocenter information, we only focus on the fit of the earthquake occurrence times by the integrated model rate over the first 4 km depth. Thus, the hydraulic diffusivity coefficient might be better constrained by previous spatiotemporal analysis of the relocated 2002 data set which resulted in estimations of $D \approx 3$ m^2/s [*Hainzl et al.*, 2006] based on a maximum likelihood model fit and $D = 0.75 \pm 0.35$ m^2/s based on distance-time plots [*Kraft et al.*, 2006a]. In addition to the parameter sensitivity, we have also tested whether our results are robust with respect to the uncertainties of the 50 focal mechanisms used in our analysis. For that purpose, we added for each focal mechanisms 10 randomly deviating mechanisms assuming standard deviations of 20° for strike, dip, and rake. Thus, we performed the parameter estimations and forecasts based on 550 instead of 50 focal mechanisms. We find that the results remain robust with changes of less than 1%.

[36] However, our model approach remains simplistic due to the lack of information about the crustal structure and detailed surface conditions. For example, we have only considered 1-D poroelastic and thermoelastic strain models, oversimplifying the local geology consisting of systems of open fractures and pronounced topography. An improved 2-D or 3-D modeling would be desirable but would require additional information such as dense measurements of the soil temperature and water flux. For the same reason, we also assumed homogeneous parameters and did not account for any nonlinear depth dependence of parameters such as hydraulic diffusivity and Young's modulus. Furthermore, because of limited information, we cannot consider the effect of snow coverage during winter months. While snowing or frozen soil inhibit or delay the water recharge at the subsurface, sudden melting might lead to strong water supply which is not included in our rainfall database. In addition, we ignored possible advective heat transport in fractures and strain-dependent hydraulic diffusivity. Because of all these simplifications, our calculations can only be expected to be a first-order approximation of the transient stresses at depth and consequently of the triggered seismicity. Thus, it is not surprising that the amplitude of rainfall-induced seismic activation varies over time and is not well correlated with our model forecasts. However, a simplified model that accounts for the key operating processes may still be able to capture the general observed features. In particular, the forecasted and modeled phases of enhanced seismicity should be correlated as observed for models ALL, RA + TE, and RA. This makes us confident that our simplified model setup represents the principles of the underlying physics. In the future, our model framework can incorporate refined stress calculations based on more detailed geological models if more observational data become available. Besides new surface measurements, additional solutions of earthquake focal mechanisms can help to better quantify the fault structure and its spatial variability. Because of the limited

number of available focal mechanisms, this is not possible so far.

[37] The overall fit of the rainfall-based models to the year 2002 seismicity is found to be very similar to that obtained by *Hainzl et al.* [2006], although the latter analysis was based only on fluid diffusion, ignoring direct loading effects of the rain amount and water accumulation. However, we cannot verify the conclusion of the previous analysis that the crust has to be in a highly critical state in this location. This conclusion depends strongly on whether or not rainfall is accumulated in open cracks as suggested by *Miller* [2008]. While the fitting quality and forecast ability of the pure rainfall model RA is found to be independent of the assumed accumulation factor f_r, the results of the combined model ALL depends on this parameter. Even without rain water accumulation ($f_r = 1$), we find that rainfall triggering dominates the triggering process with clearly positive correlations, but the fitting results for 2002 and the test scores for the period between 2003 and 2010 favor $f_r \geq 10$. For example, the information gain per earthquake for the forecast period increases from 3.1 for $f_r = 1$ to 3.6 for $f_r = 100$. For increasing values of f_r, the value of the friction parameter $A\sigma$ obtained by maximum likelihood estimation increases significantly from about 0.2 kPa in the case of no rain water accumulation up to a value of 16 kPa with $f_r = 100$. In the latter case, the value is already in the range between 0.01 and 0.2 MPa, typically found for seismicity in active tectonic areas [*Cocco et al.*, 2010; *Hainzl et al.*, 2010]. Thus, our results indicate that the local system does not have to be necessarily in a near-critical state.

7. Conclusion

[38] We test the hypothesis of rainfall triggering at Mt. Hochstaufen by analyzing new data for the years between 2003 and 2010. For that purpose, we run simulations based on rate- and state-dependent frictional earthquake nucleation in response to time-dependent stress changes induced by rainfall, surface temperature variations and Earth tides in addition to constant tectonic stressing. Although simplified, our modeling accounts for the focal earthquake mechanisms in this region and the first-order poroelastic, thermoelastic, and tidal response of the crust. Our comprehensive analysis verifies the previously observed high correlations with rainfall in the study area for 2002 [*Hainzl et al.*, 2006; *Kraft et al.*, 2006b] and more recent results of statistical correlations between meteorologic and earthquake data by *Svejdar et al.* [2011]. We find that in the examined case, the impact of rainfall is dominating the model forecasts, but accounting additionally for thermoelastic stresses can further improve the model results. In contrast, the high-frequency variations related to the Earth tides do not seem to provide a meaningful contribution. Consistent results are found for the learning period 2002 and the testing period between 2003 and 2010, where the physics-based model is found to provide earthquake forecasts with average probability gains of about 4 per event. This consistency clearly indicates the importance of rainfall-induced earthquake triggering in this region. However, the dominance of the rainfall mechanism is likely related to the large amount of rain and its amplification due to its accumulation in open fractures at Mt. Hochstaufen. The relative importance of the various processes is expected to be different in more arid regions such as Southern California.

[39] **Acknowledgments.** We are grateful for the helpful comments of Frédéric Cappa. This work was partially supported by FP7 EU-REAKT project and the Helmholtz graduate school GeoSim.

References

Agnew, D. C. (1996), *SPOTL: Some programs for ocean-tide loading, SIO Ref. Ser., 96–8*, pp. 35, Scripps Institution of Oceanography, La Jolla, Calif.

Ben-Zion, Y., and A. A. Allam (2013), Seasonal thermoelastic strain and postseismic effects in Parkfield borehole dilatometers, *Earth Planet. Sci. Lett.*, *379*, 120–126.

Ben-Zion, Y., and P. Leary (1986), Thermoelastic strain in a half-space covered by unconsolidated material, *Bull. Seismol. Soc. Am.*, *76*, 1447–1460.

Berger, J. (1975), A note on thermoelastic strains and tilts, *J. Geophys. Res.*, *80*, 274–277

Catalli, F., M. Cocco, R. Console, and L. Chiaraluce (2008), Modeling seismicity rate changes during the 1997 Umbria-Marche sequence (central Italy) through rate- and state-dependent model, *J. Geophys. Res.*, *113*, B11301, doi:10.1029/2007JB005356.

Cocco, M., and J. R. Rice (2002), Pore pressure and poroelasticity effects in Coulomb stress analysis of earthquake interactions, *J. Geophys. Res.*, *107*(B2), ESE 2-1–ESE 2-17, doi:10.1029/2000JB000138.

Cocco, M., S. Hainzl, F. Catalli, B. Enescu, A. M. Lombardi, and J. Woessner (2010), Sensitivity study of forecasted aftershock seismicity based on Coulomb stress calculation and rate- and state-dependent frictional response, *J. Geophys. Res.*, *115*, B05307, doi:10.1029/2009JB006838.

Costain, J. K., and G. A. Bollinger (2010), Review: Research results in hydroseismicity from 1987 to 2009, *Bull. Seismol. Soc. Am.*, *100*, 1841–1858, doi:10.1785/0120090288.

Daley, D. J., and D. Vere-Jones (2003), *An Introduction to the Theory of Point Processes I*, Springer, New York.

Dieterich, J. H. (1994), A constitutive law for rate of earthquake production and its application to earthquake clustering, *J. Geophys. Res.*, *99*, 2601–2618.

Dieterich, J. H., V. Cayol, and P. Okubo (2000), The use of earthquake rate changes as a stress meter at Kilauea volcano, *Nature*, *408*, 457.

Fischer, T., S. Hainzl, L. Eisner, S. A. Shapiro, and J. Le Calvez (2008), Microseismic signatures of hydraulic fracture growth in sediment formations: Observations and modeling, *J. Geophys. Res.*, *113*, B02307, doi:10.1029/2007JB005070.

Hainzl, S., and Y. Ogata (2005), Detecting fluid signals in seismicity data through statistical earthquake modeling, *J. Geophys. Res.*, *110*, B05S07, doi:10.1029/2004JB003247.

Hainzl, S., T. Kraft, J. Wassermann, and H. Igel (2006), Evidence for rain-triggered earthquake activity, *Geophys. Res. Lett.*, *33*, L19303, doi:10.1029/2006GL027642.

Hainzl, S., B. Enescu, M. Cocco, J. Woessner, F. Catalli, R. Wang, and F. Roth (2009), Aftershock modeling based on uncertain stress calculations, *J. Geophys. Res.*, *114*, B05309, doi:10.1029/2008JB006011.

Hainzl, S., G. Zöller, and R. Wang (2010), Impact of the receiver fault distribution on aftershock activity, *J. Geophys. Res.*, *115*, B05315, doi:10.1029/2008JB006224.

Hainzl, S., S. Steacy, and D. Marsan (2010), Seismicity models based on Coulomb stress calculations, Community Online Resource for Statistical Seismicity Analysis, doi:10.5078/corssa-32035809. [Available at http://www.corssa.org].

Hainzl, S., O. Zakharova, and D. Marsan (2013), Impact of aseismic transients on the estimation of aftershock productivity parameters, *Bull. Seismol. Soc. Am.*, *103*(3), 1723–1732, doi:10.1785/0120120247.

King, G. C. P., and M. Cocco (2001), Fault interaction by elastic stress changes: New clues from earthquake sequences, *Advances Geophys.*, *44*, 1–38.

Kraft, T., J. Wassermann, E. Schmedes, and H. Igel (2006a), Meteorological triggering of earthquake swarms at Mt. Hochstaufen, SE-Germany, *Tectonophysics*, *424*, 245–258.

Kraft, T., J. Wassermann, and H. Igel (2006b), High-precision relocation and focal mechanism of the 2002 rain-triggered earthquake swarms at Mt. Hochstaufen, SE Germany, *Geophys. J. Int.*, *167*, 1513–1528, doi:10.1111/j.1365-246X.2006.03171.x.

Marsan, D., E. Prono, and A. Helmstetter (2013), Monitoring aseismic forcing in fault zones using earthquake time series, *Bull. Seismol. Soc. Am.*, *103*, 169–179, doi:10.1785/0120110304.

Miller, S. A. (2008), Note on rain-triggered earthquakes and their dependence on karst geology, *Geophys. J. Int*, *173*, 334–338, doi:10.1111/j.1365-246X.2008.03735.x.

Muco, B. (1995), The seasonality of Albanian earthquakes and crosscorrelation with rainfall, *Phys. Earth Planet. Int.*, *88*, 285–291.

Niu, G.-Y., Z.-L. Yang, R. E. Dickinson, L. E. Gulden, and H. Su (2007), Development of a simple groundwater model for use in climate models and evaluation with gravity recovery and climate experiment data, *J. Geophys. Res.*, *112*, D07103, doi:10.1029/2006JD007522.

Ogata, Y. (1988), Statistical models for earthquake occurrence and residual analysis for point processes, *J. Am. Stat. Assoc.*, *83*, 9–27.

Prawirodirdjo, L., Y. Ben-Zion, and Y. Bock (2006), Observation and modeling of thermoelastic strain in SCIGN daily position time series, *J. Geophys. Res.*, *111*, B02408, doi:10.1029/2005JB003716.

Roeloffs, E. A. (1988), Fault stability changes induced beneath a reservoir with cyclic variations in water level, *J. Geophys. Res.*, *93*, 2107–2124.

Shapiro, S. A., R. Patzig, E. Rothert, and J. Rindschwentner (2003), Triggering of seismicity by pore-pressure perturbations: Permeability-related signatures of the phenomenon, *Pure Appl. Geophys.*, *160*, 1051–1066.

Simpson, G. (2001), Influence of compression-induced fluid pressures on rock strength in the brittle crust, *J. Geophys. Res.*, *106*, 19,465–19,478.

Svejdar, V., H. Küchenhoff, L. Fahrmeir, and J. Wassermann (2011), External forcing of earthquake swarms at Alpine regions: Example from a seismic meteorological network at Mt. Hochstaufen SE-Bavaria, *Non. Proc. Geophys.*, *18*, 849–860, doi:10.5194/npg-18-849-2011.

Talwani, P. (1997), On the nature of reservoir-induced seismicity, *Pure Appl. Geophys.*, *150*, 473–492.

Thomas, A. M., R. M. Nadeau, and R. Bürgmann (2009), Tremor-tide correlations and near-lithostatic pore pressure on the deep San Andreas fault, *Nature*, *462*, doi:10.1038/nature08654.

Toda, S., R. S. Stein, P. A. Reasenberg, J. H. Dieterich, and A. Yoshida (1998), Stress transferred by the 1995, M_w=6.9 Kobe, Japan, shock: Effect on aftershocks and future earthquake probabilities, *J. Geophys. Res.*, *103*(B10), 24,543–24,565.

Utsu, T., Y. Ogata, and R. S. Matsu'ura (1995), The centenary of the Omori formula for a decay of aftershock activity, *J. Phys. Earth*, *43*, 1–33.

Weede, M. (2002), Die Geologie des Hochstaufen unter besonderer Berücksichtigung der Massenbewegungen, Diploma Thesis, Technical Univ. of Munich.

Xu, C., J. Wang, Z. Li, and J. Drummond (2010), Applying the Coulomb failure function with an optimally oriented plane to the 2008 Mw 7.9 Wenchuan earthquake triggering, *Tectonophysics*, *491*, 119–126.

Zoback, M. D., and H.-P. Harjes (1997), Injection-induced earthquakes and crustal stress at 9 km depth at the KTB deep drilling site, Germany, *J. Geophys. Res.*, *102*, 18,477–18,492.